APL Materials

Ideal simple shear strengths of two HfNbTaTi-based quinary refractory multi-principal element alloys

Cite as: APL Mater. **10**, 111107 (2022); https://doi.org/10.1063/5.0116898
Submitted: 30 July 2022 • Accepted: 05 October 2022 • Published Online: 08 November 2022

Shuozhi Xu, Wu-Rong Jian and Irene J. Beyerlein

Ideal simple shear strengths of two HfNbTaTi-based quinary refractory multi-principal element alloys

Cite as: APL Mater. 10, 111107 (2022); doi: 10.1063/5.0116898
Submitted: 30 July 2022 • Accepted: 5 October 2022 •
Published Online: 8 November 2022

Shuozhi Xu,[1,a)] Wu-Rong Jian,[2] and Irene J. Beyerlein[1,3]

AFFILIATIONS

[1] Department of Mechanical Engineering, University of California, Santa Barbara, California 93106-5070, USA
[2] Department of Mechanical Engineering, Stanford University, Stanford, California 94305, USA
[3] Materials Department, University of California, Santa Barbara, California 93106-5050, USA

Note: This paper is part of the Special Topic on Design and Development of High Entropy Materials.
[a)] **Author to whom correspondence should be addressed:** shuozhixu@ucsb.edu

ABSTRACT

Atomistic simulations are employed to investigate chemical short-range ordering in two body-centered cubic refractory multi-principal element alloys, HfMoNbTaTi and HfNbTaTiZr, and its influence on their ideal simple shear strengths. Both the alias and affine shear strengths are analyzed on the {110} and {112} planes in the two opposing ⟨111⟩ directions. In both quinary alloys, local ordering of NbNb, TaTa, HfNb, HfTa, and NbTa is preferred as the annealing temperature decreases from 900 to 300 K. The pair that achieves the highest degree of local ordering is TiTi in HfMoNbTaTi and HfTi in HfNbTaTiZr. Subject to the affine shear, these alloys yield by first phase transformation at the most likely pairs followed by deformation twinning at those sites.

I. INTRODUCTION

Refractory multi-principal element alloys (RMPEAs) have been identified as promising candidate materials for aerospace propulsion systems, land-based gas turbines, nuclear reactors, heat exchanger tubing, and the chemical process industry.[1] These materials consist of at least three metallic elements with equal- or near-equal molar ratio with most or all constituent elements being refractory metals.[2] Two equal-molar quinary RMPEAs, HfMoNbTaTi and HfNbTaTiZr, possess outstandingly high room temperature (RT) strengths. Take the compressive yield strength as an example. It is 1369–1713 MPa for of HfMoNbTaTi[3,4] and 900–1073 MPa for HfNbTaTiZr.[5–9] Unlike pure refractory metals, many RMPEAs can retain ultra-high strengths over a broad range of elevated temperatures. For example, the compressive yield strength of HfMoNbTaTi decreases from 1369 MPa to 699 MPa (i.e., −49%) when the temperature increases from RT to 1473 K.[3] The percentage decrease is smaller than those in pure refractory metals. For example, in Nb and Ta, the ultimate tensile strengths at RT, 290 and 441 MPa, respectively, decrease to 65 and 106 MPa at 1473 K.[10] The relative change is −78% in Nb and −76% in Ta.

The high temperature strengths of RMPEAs, e.g., 699 MPa for HfMoNbTaTi at 1473 K,[3] are impressive, when compared to those of six currently used Ni-based superalloys, 115–185 MPa at the same temperature.[11] The other alloy, HfNbTaTiZr, is one of the few RMPEAs that has sufficient RT tensile ductility, being 11%–25%.[9,12–14] The ductility of its subsets is also high, e.g., HfNbTa (10%),[15] HfNbTaTi (11%),[15] $Hf_{27.5}Nb_5Ta_5Ti_{35}Zr_{27.5}$ (23%),[16] HfNbTiZr (14%–15%),[17,18] $HfTa_{0.5}TiZr$ (27%),[19] and NbTaTi (19%).[15]

One characteristically intriguing feature of RMPEAs is their lack of chemical long-range ordering. In the meantime, many RMPEAs have been found to exhibit chemical short-range ordering (CSRO) that influences dislocation dynamics in these alloys.[20–24] Using atomistic simulations in HfNbTaZr, the slip resistance of an edge dislocation was found to increase with CSRO.[24] In another RMPEA, NbTiZr, greater CSRO led to slightly lower shear stress to move a screw dislocation.[22] Atomistic simulations have been

used widely for strength studies in body-centered cubic (BCC) MPEAs but mostly for non-RMPEAs[25–30] and with a few exceptions for RMPEAs, including MoTaTiWZr, to calculate their tensile and compressive strengths,[31,32] and AlMoTaW[33] and MoNbTaW,[20] to determine their compressive strengths.

In this article, using atomistic simulations, we investigate the effect of CSRO on the ideal shear strengths of HfMoNbTaZr and HfNbTaTiZr. We show that five atomic pairs—NbNb, TaTa, HfNb, HfTa, NbTa—tend to segregate in both RMPEAs. Increasing levels of CSRO affect not only the ideal shear strength but also the asymmetry in the two opposing shear directions.

II. MATERIALS AND METHODS

A. Interatomic potentials

Embedded-atom method (EAM) potentials[42] are used to describe the interatomic interactions. The six elemental potentials are Hf,[43] Mo,[44] Nb,[45] Ta,[44] Ti,[44] and Zr[44] and the cross interactions among these elements are based on the formulations by Johnson[46] and Zhou *et al.*[47] The resulting interatomic potentials built for the HfMoNbTaTi and HfNbTaTiZr RMPEAs are referred to hereinafter as the alloy potentials. Based on them, we construct two *A*-atom potentials, which provide mean-field representations of the RMPEAs,[48] resulting in two artificial pure metals, denoted as HfMoNbTaTi$_A$ and HfNbTaTiZr$_A$, respectively. Except the HfNbTaTiZr alloy potential,[43] all four potentials are newly developed here. They can be downloaded at https://github.com/shuozhixu/APLmater_2022.

To assess the accuracy of these potentials, we performed density functional theory (DFT) calculations for the lattice parameters (a_0) and effective BCC elastic constants ($C_{11}^{\dagger}$, $C_{12}^{\dagger}$, $C_{44}^{\dagger}$) for the random structures of the two RMPEAs and compared these quantities with those from the alloy potentials. The atomistic and DFT calculations here are performed via Large-scale Atomic/Molecular Massively Parallel Simulator (LAMMPS)[49] and Vienna *Ab initio* Simulation Package (VASP),[50] respectively, following our previous work.[41] We also compare the alloy potential-based results with available DFT or experimental data in the literature. In Table I, it is found that the alloy potentials generally well predict the structural parameters compared with the present and prior DFT results. In particular, our HfNbTaTiZr alloy potential, which yields $C_{12}^{\dagger}$ = 111.83 GPa, performs better than a modified EAM potential,[34] which yields a much smaller $C_{12}^{\dagger}$ (69.09 GPa) than experimental (116 GPa) and DFT values (118.27–124.4 GPa).

TABLE I. Lattice parameters a_0 (in Å) and effective BCC elastic constants $C_{11}^{\dagger}$, $C_{12}^{\dagger}$, $C_{44}^{\dagger}$ (in GPa) of different models in two RMPEAs. Superscripts § and ‡ denote data from experiments and DFT calculations, respectively. Models without superscripts are from atomistic simulations of size D structures in Table II, among which one set of data is based on a modified EAM potential of HfNbTaTiZr.[34] All unreferred data from DFT or alloy potentials are newly calculated here, where a_0 and $C_{ij}^{\dagger}$ are obtained using the energy–volume method[35] and stress–strain method,[36] respectively. Data of three constituent BCC pure metals, based on the elemental interatomic potentials, are also presented as references. Experimental and computational elastic constants were based on polycrystals and single-crystals, respectively.

Material		a_0	$C_{11}^{\dagger}$	$C_{12}^{\dagger}$	$C_{44}^{\dagger}$
HfMoNbTaTi	Random§	3.305[3,4]			
	Random‡	3.305	209.95	133.92	39.68
	Random	3.31	201.42	146.64	82
	900KMDMC	3.311	186.19	121.8	82.07
	600KMDMC	3.311	222.1	157.91	82.38
	300KMDMC	3.31	202.89	138.51	82.49
	A-atom	3.311	212.33	143.09	89.6
HfNbTaTiZr	Random§	3.404[5]	172[37]	116[37]	28[37]
	Random‡	3.457[38]	160.2[38]	124.4[38]	62.4[38]
	Random‡	3.398[39]	158.1[40]	121.9[40]	62.2[40]
	Random‡	3.391	150.79	118.27	38.86
	Random[34]	3.425	197.96	69.09	77.87
	Random	3.405	149.63	111.83	64.67
	900KMDMC	3.405	159.03	118.75	67.51
	600KMDMC	3.405	159.75	118.94	67.53
	300KMDMC	3.405	166.62	119.65	68.14
	A-atom	3.408	162.23	118.59	73.55
Mo		3.135[41]	458.76[41]	167.84[41]	114.32[41]
Nb		3.3[41]	263.56[41]	125.28[41]	35.03[41]
Ta		3.303[35]	262.59[35]	157.74[35]	82.33[35]

B. Ideal shear strength

Generally, the ideal shear strength is the minimum stress needed to plastically deform an infinite defect-free material and is an upper bound to the shear strength of the material.[51,52] It is not related to the shear strength of a material that already contains defects. There are two types of ideal shear: the alias shear and the affine shear.[53] The alias shear strength is related to the potential energy to displace two crystalline halves across a given slip plane. The affine shear strength allows the entire crystal to deform to accommodate the homogeneously applied shear. In each type, the applied shear can be either a pure shear or simple shear. These different types of shear calculations have been compared for pure face-centered cubic (FCC) metals[52–55] and FCC MPEAs,[56] revealing that (i) the simple shear strength is higher than the pure shear strength and (ii) the affine shear strength is higher than the alias one. The first statement was found to hold in pure BCC metals.[54,57] However, the affine and alias shear strengths have not been compared in any pure BCC metals or RMPEAs. Here, we consider both alias and affine shear strengths in simple shear. Compared with the pure shear strength, the simple shear strength is more closely related to the slip resistance for a dislocation when the shear plane is selected as the glide plane.[58] Between the two RMPEAs studied here, dislocations were experimentally investigated only in HfNbTaTiZr,[7,9,59] suggesting that screw dislocations on {110} and {112} planes are prevalent. Our recent atomistic modeling work in six RMPEAs also showed that these two planes are operative during plastic deformation.[36,60,61] Therefore, two shear planes, {110} and {112}, are considered in this work.

1. Simulation cells for the RMPEAs

We first construct special quasi-random structures (SQSs) in which the five elements are randomly distributed[62] using ATAT.[63]

TABLE II. Edge lengths of eight SQS simulation cells, L_x, L_y, and L_z, for HfMoNbTaTi, in Å. The cells for random HfNbTaTiZr structure or any RMPEA with CSRO have the same number of atoms, but the edge lengths are scaled with respect to its a_0. The cross-sectional area of the shear plane, $A_{ij} = L_i L_j$, in nm^2. Note that for sizes D and E, the {110} and {112} cells have the same L but different A.

Size		A	B	C	D	E
{110}	L_x	270.56	272.03	271.56	135.77	271.52
	L_y	8.1	24.33	32.44	137.84	275.66
	L_z	2.89	20.07	31.53	137.61	272.29
	A_{yz}	0.23	4.88	10.23	189.68	750.59
{112}	L_x	4.66	23.41	32.77	135.77	271.52
	L_y	275.84	275.56	275.75	137.84	275.66
	L_z	2.89	20.07	31.54	137.61	272.29
	A_{xz}	0.13	4.7	10.34	186.83	739.32

The crystallographic orientations are always ⟨110⟩, ⟨112⟩, and ⟨111⟩ along x, y, and z directions, respectively. Five different simulation cell sizes (A–E), summarized in Table II, are considered. For each RMPEA, there are two size A, two size B, and two size C cells, in which either L_x or L_y is the largest cell edge length. For the larger cells considered, size D and size E, there is only one size.

Two size C and one size D cells are employed to generate structures with CSRO. We first determine the chemical potential differences between Nb and the other five elements under the semi-grand-canonical (SGC) ensemble at 1500 K via the hybrid molecular dynamics (MD)/Monte Carlo (MC) technique using a small cubic cell containing 2000 atoms. The values obtained are summarized in Table S1 in the supplementary material. Next, based on cells of size C or size D, we perform hybrid MD/MC simulations under the variance-constrained SGC (VCSGC) ensemble at three annealing temperatures of 300, 600, and 900 K, respectively. Each MC cycle is accompanied by 20 MD steps. After 600 000 MC cycles, the potential energy converges to a constant, and so the equilibrium configurations with the equal-molar composition and thermodynamically correct occupation of atomic sites are achieved. The last step is to quench these structures to 1 K and to minimize the system energy with all three normal stresses being zero. More details of the hybrid MD/MC simulations can be found in our previous work.[65] As a result, for each RMPEA, we obtain nine atomic structures with CSRO, in addition to the eight random ones in Table II. Eight size C atomistic structures in the two RMPEAs are presented in Fig. 1. Note that the parallel algorithm under the VCSGC ensemble requires that each edge length of the simulation cell must be no less than four times the cutoff radius of the EAM potential,[66] 28.62 Å, thus excluding size A and size B cells.

CSRO is measured using the nearest neighbor shell-based Warren–Cowley (WC) parameters:

$$\alpha_{ij} = \frac{p_{ij} - c_j}{\delta_{ij} - c_j}, \tag{1}$$

where p_{ij} denotes the probability of a j-type atom being around an atom of type i within the shell, c_j is the concentration of j-type atom, and δ_{ij} is the Kronecker delta function.[67,68] Note that $\alpha_{ij} = \alpha_{ji}$ in equal-molar MPEAs. In a completely random structure, $\alpha_{ij} = 0$ for all ij pairs. A tendency for segregation or local ordering corresponds to a positive α_{ij} for pairs of the same species (i.e., $i = j$) or a negative α_{ij} for those of different species (i.e., $i \neq j$). In either case, a higher α_{ij} magnitude suggests a higher degree of CSRO.

In what follows, we use "number+K+MDMC" to denote the structure obtained by hybrid MD/MC simulations at a specific annealing temperature. For example, "600KMDMC" represents the structure created by hybrid MD/MC simulations at 600 K. The values of structural parameters of size D structures with CSRO are provided in Table I. In general, the presence of CSRO influences $C_{11}^{\dagger}$, $C_{12}^{\dagger}$, and $C_{44}^{\dagger}$ much more than it does a_0.

2. Alias simple shear strength

The alias simple shear strength, T_{al}, is the maximum stress for the sliding between two adjacent atomic planes along a certain direction. In BCC metals, T_{al} has been related to the generalized stacking fault energy (GSFE) curve γ_{gsf}.[69,70] All eight random structures and three structures with CSRO are used to calculate γ_{gsf}. A 20 Å thick vacuum is added, along the x and y directions, respectively, to the {110} and {112} cells (Table II). Along all directions, periodic boundary conditions (PBCs) are applied. The top atomic planes are displaced by d with respect to the bottom ones along the $z\langle 111\rangle$ direction. Following each displacement, energy minimization is performed, in which the top two and bottom two atomic planes are fixed while the remaining ones are allowed to move along the x and y direction, respectively, in {110} and {112} cell. A GSFE curve is then obtained as a function of d from 0 to $\sqrt{3}a_0/2$. More details of the GSFE calculations in RMPEAs can be found in Refs. 36 and 41, which were focused on random solid solutions. The procedure is repeated for several parallel planes with distinct atomic arrangements. We obtain 80 $\gamma_{\mathrm{gsf}}^{110}$ curves and 100 $\gamma_{\mathrm{gsf}}^{112}$ curves for each cell in each RMPEA. Each GSFE curve exhibits a single peak value, called the unstable SFE γ_{usf}, i.e.,

$$\gamma_{\mathrm{usf}} = \max[\gamma_{\mathrm{gsf}}(d)]. \tag{2}$$

In pure BCC metals, the {112} plane exhibits a geometric asymmetry in shear resistance in the twinning (soft) and anti-twinning (hard) ⟨111⟩ directions. In RMPEAs, the fluctuations in composition across the glide plane can induce a chemical asymmetry in the resistance to shear between positive and negative ⟨111⟩ directions, even for the {110} plane.[41] Here, we use $T_{\mathrm{al\text{-}s}}$ to denote the soft sense and $T_{\mathrm{al\text{-}h}}$ the hard sense, as defined by

$$T_{\mathrm{al-s}} = \max\left|\frac{\partial \gamma_{\mathrm{gsf}}(d)}{\partial d}\right|, \quad 0 \le d < \sqrt{3}a_0/4, \tag{3}$$

$$T_{\mathrm{al-h}} = \max\left|\frac{\partial \gamma_{\mathrm{gsf}}(d)}{\partial d}\right|, \quad \sqrt{3}a_0/4 \le d < \sqrt{3}a_0/2. \tag{4}$$

3. Affine simple shear strength

To calculate the affine simple shear strength T_{af}, four size D cells—one SQS and three structures with distinct CSRO—are adopted for each RMPEA. Size D, instead of size C, is chosen because it is sufficiently large to accommodate possible defect nucleation and

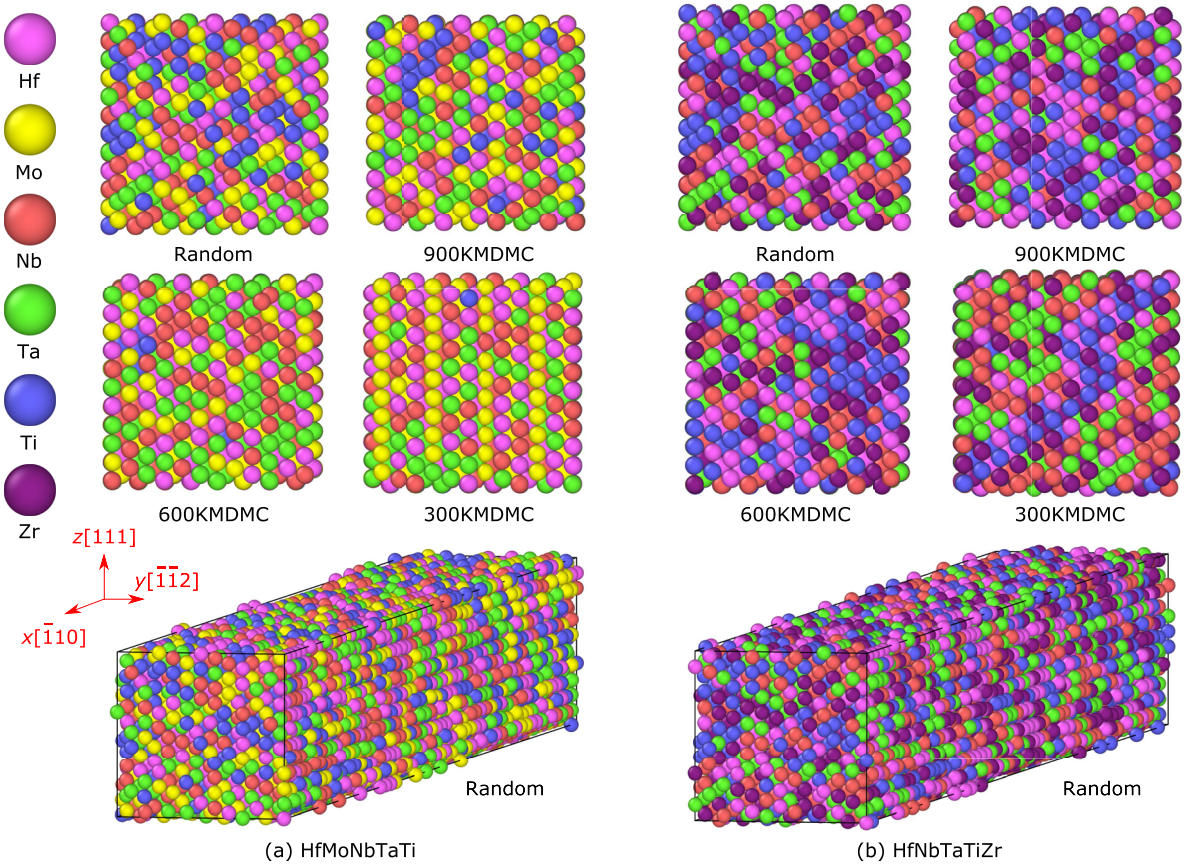

FIG. 1. Atomistic structures of size C cells for two RMPEAs with or without CSRO. For each RMPEA, the top four snapshots are the projections of the structures onto the *yz* plane. Visualization is done in OVITO.[64]

evolution. PBCs are applied to all directions. An affine simple shear is applied to each cell, with the stress–strain response recorded. The shear plane is either {110} or {112}, while the shear direction is one of the two opposite ⟨111⟩ directions. T_{af} corresponds to the peak stress in the stress–strain curve, when defects (e.g., dislocations and twins) or phase transformation (PT) start to emerge within the crystal. Similar to T_{al}, T_{af} possesses a soft and hard sense, i.e., $T_{af\text{-}s}$ and $T_{af\text{-}h}$, for each plane in each structure. To assess temperature and strain rate effects, calculations for a few selected cases are repeated over a series of strain rates from 5×10^7 s^{-1} to 5×10^{11} s^{-1} and temperatures from 0 to 300 K. Figures S1 and S2 of the supplementary material show that T_{af} converges for strain rates $\leq 5 \times 10^8$ s^{-1} and decreases linearly with increasing temperature. Unless stated otherwise, most simulations in the current work are carried out at 5×10^8 s^{-1} and 1 K, at which the CSRO effects are important. A total of four T_{af} are obtained for each sense on each plane in each RMPEA.

For reference, T_{al} and T_{af} of five pure metals—two *A*-atom ones, $HfMoNbTaTi_A$, $HfNbTaTiZr_A$, and three BCC constituents, Mo, Nb, and Ta—are also calculated using similar procedures. Results of the last three metals are summarized in Table S2 in the supplementary material.

III. RESULTS AND DISCUSSION

A. Size effects in the alias shear strength

Calculating γ_{usf} and T_{al} requires selecting a cross-sectional area *A*. Figure 2 shows the effect of *A* on the average ($\bar{T}_{al}$) and standard deviation in T_{al} (S_{al}) for two RMPEAs. For the broad range of sizes considered, *A* is found to have a small effect on $\bar{T}_{al}$, with a <3% variation for HfMoNbTaTi and <6% for HfNbTaTiZr. The standard deviation S_{al}, on the other hand, is affected by *A* and decreases with increasing *A*. These size effects are similar to those found in a study on the intrinsic SFE in FCC equal-molar FeNi binary and unequal-molar CrFeNi MPEA.[71,72] Here, the size effect is relevant and strong when $A \leq 1$ nm^2, about the size of a dislocation core. In this regime, HfMoNbTaTi has a larger standard deviation, but similar coefficient of variation, with respect to HfNbTaTiZr. Compared to the {110} planes, the {112} planes have the greater coefficient of variation (0.2–0.22 compared to 0.27–0.31). Once *A* is above 100 nm^2, differences in S_{al} between the two shear planes {110} and {112} and two RMPEAs become negligible, within 0.05 GPa. Similar trends are found for the average γ_{usf} and standard deviation in γ_{usf} as shown in Fig. S3 of the supplementary material.

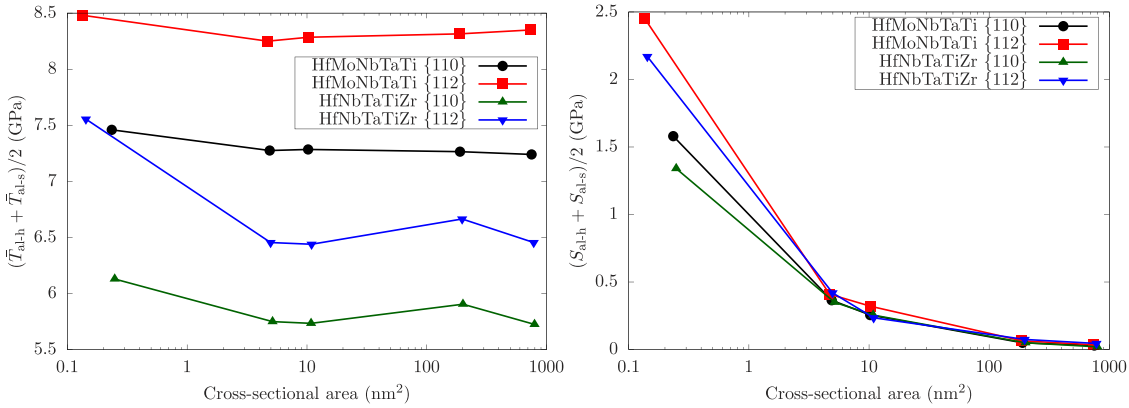

FIG. 2. (a) Averaged value of T_{al} and (b) averaged standard deviation S_{al} in random structures of two RMPEAs as a function of the cross-sectional area.

The size effect is also examined for the quinaries with CSRO by repeating the γ_{usf} and T_{al} calculations for structures of sizes C and D. Since the chemical ordering is short-range, the influence of changing CSRO is expected to diminish for the larger A. We find that for the random and 900KMDMC cases, the values are the same between the two sizes. For 600KMDMC and 300KMDMC, the effects of CSRO are slightly subdued with the larger size D. Apart from this, CSRO does not change the fact that the quinaries have lower $\bar{\gamma}_{usf}$ and $\bar{T}_{al}$ than the three BCC constituents, that HfMoNbTaTi has higher $\bar{\gamma}_{usf}$ and $\bar{T}_{al}$ values than HfNbTaTiZr, and that the standard deviation for size D is lower than that for size C. The last point is demonstrated in Fig. S4 in the supplementary material.

B. CSRO

The WC parameters for all possible pairs in both quinaries are provided in Tables S3 and S4 in the supplementary material. At the lowest annealing temperature of 300 K, results for HfNbTaTiZr show that NbNb, TaTa, HfNb, HfTa, HfTi, NbTa, NbZr, TaZr, and TiZr pairs are likely, while in HfMoNbTaTi, the NbNb, TaTa, TiTi, HfMo, HfNb, HfTa, MoNb, MoTa, and NbTa pairs would tend to segregate. In general, the median of the absolute WC parameter values is higher for HfNbTaTiZr than for HfMoNbTaTi. In the 300KMDMC case, for instance, the median is 0.224 for HfMoNbTaTi compared to 0.242 for HfNbTaTiZr. Figure 3 shows the evolution of the five most significantly favored elemental pairs in the two RMPEAs, as the annealing temperature decreases. The most favored pair is TiTi and HfTi, respectively, in HfMoNbTaTi and HfNbTaTiZr.

Between the two RMPEAs, the CSRO in only HfNbTaTiZr has been previously investigated. Experiments have found segregation of the NbTa pair between 773 and 1073 K[9,13,73–76] and the HfTa pair between 873 and 1073 K.[77] At a high temperature of 2773 K, *ab initio* MD simulations found that CSRO is absent.[78] Based on a modified EAM potential,[34] Huang *et al.*[79] showed that four unlike atomic pairs tend to segregate at 800 K: HfTi, HfZr,

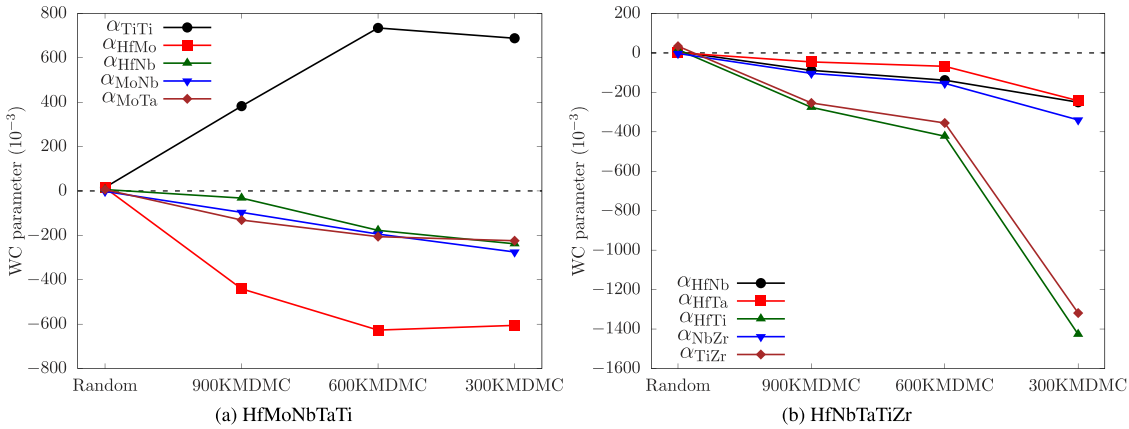

FIG. 3. Changes in the five most significant WC parameters with annealing temperature in two RMPEAs.

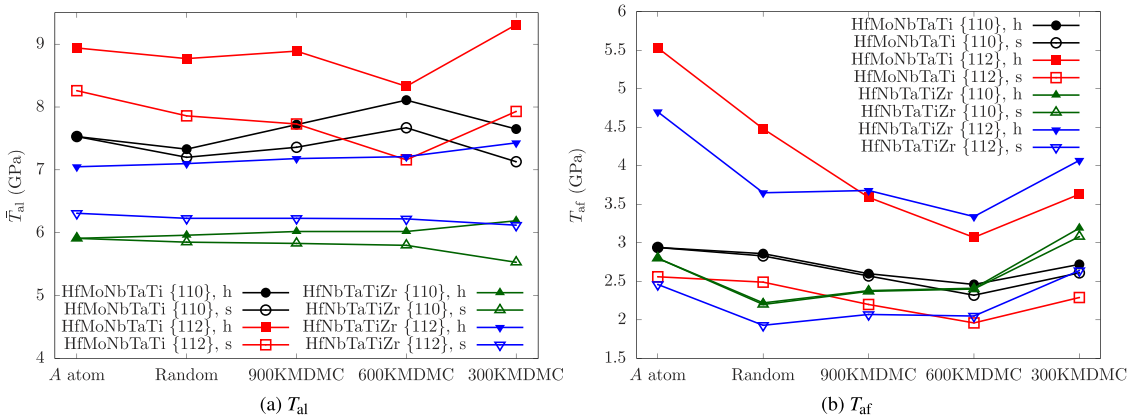

(a) $\bar{T}_{al}$ (b) T_{af}

FIG. 4. (a) Alias simple shear strength and (b) affine simple shear strength, in structures of size D in two RMPEAs with or without CSRO. "h" and "s" denote hard and soft senses, respectively.

NbTa, and TiZr. First principles calculations at 1002 and 1298 K[80] and CALPHAD modeling between 273 and 1073 K[75] identified segregation of HfZr and NbTa pairs. First principles calculations also predicted TaTa clustering at 886 K and ZrZr clustering at 1023 K.[80] The only two discrepancies between the present work and first principles calculations pertain to ZrZr and HfZr. These are likely owing to the difference in the interatomic potential or the cell size used.

C. CSRO effects on shear strength

Figure 4 presents both $\bar{T}_{al}$ and T_{af} of two RMEPAs with CSRO attained at three different annealing temperatures. The evolution of the strengths in the hard and soft senses is tracked individually. We include for reference the strengths of the *A*-atom versions of these RMPEAs, which are found to provide a good estimate of $\bar{T}_{al}$, but not T_{af}, with respect to the random alloy.

We first discuss the alias shear strength. $\bar{T}_{al}$ values for HfMoNbTaTi are higher than those for HfNbTaTiZr, a reflection of the fact that Mo is stronger than Zr. For both quinaries, in the case of *A*-atom pure metal and random alloy, which have no CSRO, $\bar{T}_{al}$ on the {112} plane is higher than that on the {110} one. In HfNbTaTiZr, with an increasing CSRO, $\bar{T}_{al}$ only slightly increases in the hard sense, while decreasing in the soft sense. In HfMoNbTaTi, the influence of CSRO is more noticeable, yet it is not consistent for the two shear planes. For example, when the annealing temperature decreases from 600 to 300 K, $\bar{T}_{al}$ on the {110} plane decreases, while that on the {112} plane increases. The anisotropy in CSRO effects, exhibited for different senses or planes, is intriguing. It may be a result of the anisotropic clustering/segregation during the annealing. For both quinaries, increasing the CSRO levels tends to increase the asymmetry between the hard and soft senses. Overall, the CSRO effects on $\bar{T}_{al}$ are relatively weak. On the other hand, prior atomistic simulations showed that T_{al} is positively correlated with the local slip resistance in pure refractory metals[70] and RMPEAs.[36,60] These suggest that the CSRO effects on slip resistance are weak in RMPEAs, consistent with prior atomistic studies.[20–24]

Next, we discuss the affine shear strength. T_{af} values for the *A*-atom pure metals and RMPEAs exhibit the expected anisotropy with the {112} strength in the hard sense being greater than the {110} strength and both greater than the {112} strength in the soft sense. Moreover, compared with T_{al}, T_{af} is less sensitive to the bulk composition. However, both quinaries display similar trends in T_{af} with increasing CSRO level. For example, when the annealing temperature decreases from 900 to 300 K, T_{af} increases in both RMPEAs.

The mechanism of affine shear deformation is not concentrated to a single plane in the crystal and in fact could be unrelated to dislocation motion. Thus, its deformation mechanisms are completely different from that presumed by alias shear. For example, subject to the affine simple shear, both Mo and Nb yield via the homogeneous nucleation of twins, as shown in Fig. 5(a). The same yielding mechanism was reported in tensile loading of a Mo single crystal using the same interatomic potential employed here.[32] In Ta, as well as the two *A*-atom materials, yield occurs first by a BCC-to-FCC phase transformation (PT) followed by homogeneous nucleation of twins, as shown in Fig. 5(b). A similar BCC-to-FCC PT was reported in shearing of Fe using atomistic simulations.[82] Both RMPEAs, with or without CSRO, yield first by a BCC-to-FCC PT in local regions followed by twinning in those same regions. In HfMoNbTaTi, Ti atoms tend to form clusters and initial local PT takes place at the boundaries of the Ti-rich regions, as shown in Fig. 5(c). Likewise, in HfNbTaTiZr, the HfTi pair tends to segregate and initial local PT occurs in these HfTi-rich regions. Between the two RMPEAs, deformation twinning was experimentally observed in HfNbTaTiZr,[5] but not yet in the other alloy.

CSRO effects on deformation of RMPEAs have been studied previously only for polycrystals using experiments (exp) or MD simulations, where CSRO was found to increase the tensile strength in HfNbTaTiZr (exp)[9] and MoNbTaW (MD)[20] as well as hardness and compressive strength in HfNbTaZr (exp).[83] Although shear deformation was not explicitly studied, results from uniaxial deformation indicate that CSRO likely increases T_{af}. Recent atomistic simulations in FCC CoCrNi MPEA[84] have found that CSRO promotes the

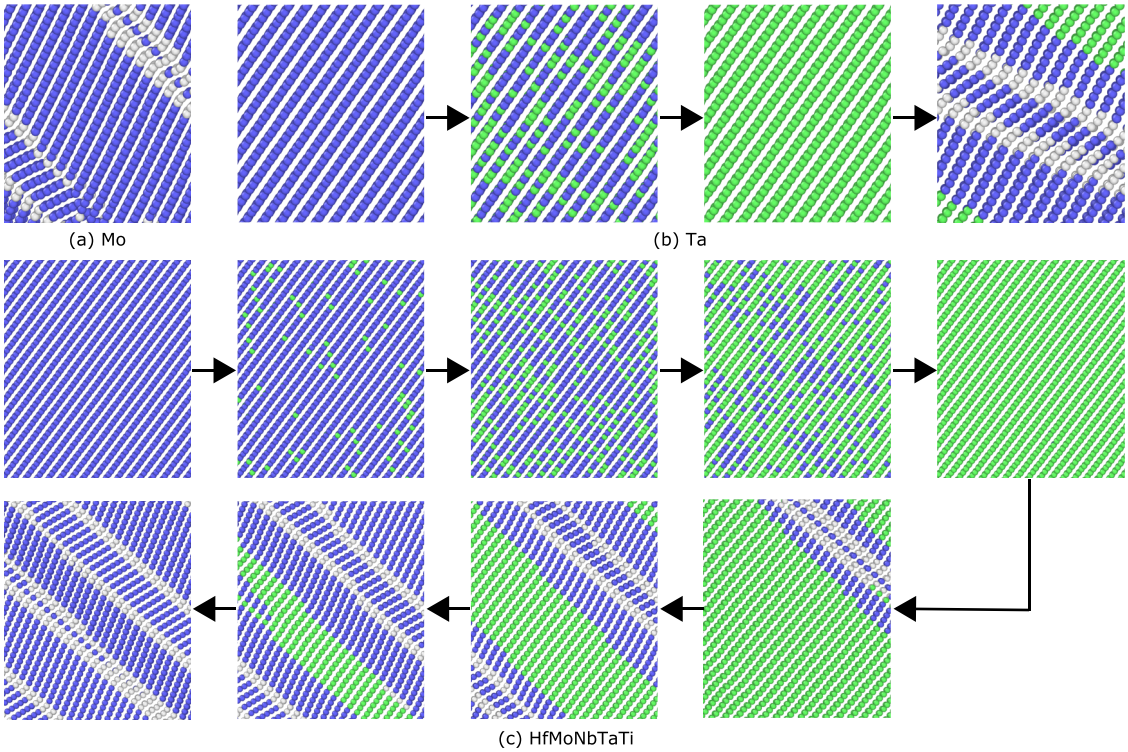

FIG. 5. BCC-to-FCC phase transformation and/or deformation twinning taking place in (a) Mo, (b) Ta, and (c) HfMoNbTaTi. Visualization is done in OVITO.[64] Based on the adaptive common neighbor analysis,[81] blue, green, and white correspond to BCC, FCC, and disordered local lattice structures, respectively.

FCC-to-BCC PT, which suggests that it may decrease T_{af}. CSRO was also shown to increase γ_{usf} in two BCC RMPEAs, MoNbTi and TaNbTi,[85] suggesting that it might promote T_{al}. Here, our simulations show that higher levels of CSRO have different effects on T_{al} and T_{af} in RMPEAs. For both strengths, the CSRO effects are not influenced by either the cross-sectional area or temperature, a conclusion that can be reached if one compared Fig. 4 with Fig. S5 in the supplementary material.

Finally, for the same sense on the same plane in the same RMPEA, T_{al} is plotted with respect to T_{af} in Fig. S6 in the supplementary material. It is shown that the two strengths are loosely correlated, with higher T_{al} corresponding to higher T_{af} and vice versa. The weak relationship may be expected since the mechanisms accommodating deformation in each type are different, in either pure metals or RMPEAs.

IV. CONCLUSIONS

In this article, we conduct atomistic simulations to calculate the alias (T_{al}) and affine (T_{af}) ideal simple shear strengths in two quinary RMPEAs, HfMoNbTaTi and HfNbTaTiZr, with or without CSRO. The strengths in two opposing ⟨111⟩ directions on both {110} and {112} planes are calculated. For reference, the same strengths of the constituent elements Mo, Nb, and Ta, as well as hypothetical A-atom homogeneous versions of HfMoNbTaTi and HfNbTaTiZr, are also calculated. The main findings are summarized as follows:

1. The interatomic potentials for both RMPEAs are validated by comparing the corresponding lattice parameters and elastic constants against those from DFT and experimental data.
2. The size of the cross-sectional area A does not affect the average T_{al} much. However, a smaller A increases the standard deviation in T_{al}.
3. The two RMPEAs possess much lower T_{al} and T_{af} than the constituent BCC metals: Mo, Nb, and Ta.
4. In both RMPEAs, five atomic pairs, NbNb, TaTa, HfNb, HfTa, and NbTa, tend to segregate. The degree of CSRO increases with decreasing annealing temperature. The most likely pairing is TiTi in HfMoNbTaTi and HfTi in HfNbTaTiZr.
5. Subject to affine simple shear deformation, the two RMPEAs yield by two steps: first a BCC-to-FCC PT followed by twinning. In HfMoNbTaTi, the PT preferentially occurs at the boundaries of Ti clusters, whereas in HfNbTaTiZr the PT tends to initiate in the HfTi-rich regions.

SUPPLEMENTARY MATERIAL

See the supplementary material for information as referred to in the main text.

ACKNOWLEDGMENTS

We thank Dr. Prashant Singh for helpful discussions. S.X. and I.J.B. gratefully acknowledge support from the Office of Naval Research under contract ONR BRC Grant No. N00014-21-1-2536. W.-R.J. would like to acknowledge funding from the Office of Naval Research under Grant No. N00014-17-1-2810. We acknowledge the use of computational facilities purchased with funds from the National Science Foundation (Grant No. CNS-1725797) and administered by the Center for Scientific Computing (CSC). The CSC is supported by the California NanoSystems Institute and the Materials Research Science and Engineering Center (MRSEC; Grant No. NSF DMR 1720256) at UC Santa Barbara.

AUTHOR DECLARATIONS

Conflict of Interest

The authors have no conflicts to disclose.

Author Contributions

Shuozhi Xu: Conceptualization (equal); Data curation (lead); Formal analysis (lead); Investigation (lead); Methodology (lead); Visualization (lead); Writing – original draft (lead); Writing – review & editing (equal). **Wu-Rong Jian**: Methodology (supporting); Resources (supporting); Validation (lead); Writing – review & editing (supporting). **Irene J. Beyerlein**: Conceptualization (equal); Funding acquisition (lead); Supervision (lead); Writing – review & editing (equal).

DATA AVAILABILITY

The data that support the findings of this study are available from the corresponding author upon reasonable request.

REFERENCES

[1] O. N. Senkov, D. B. Miracle, K. J. Chaput, and J.-P. Couzinié, "Development and exploration of refractory high entropy alloys—A review," J. Mater. Res. **33**, 3092–3128 (2018).

[2] O. N. Senkov, G. B. Wilks, D. B. Miracle, C. P. Chuang, and P. K. Liaw, "Refractory high-entropy alloys," Intermetallics **18**, 1758–1765 (2010).

[3] K.-K. Tseng, C.-C. Juan, S. Tso, H.-C. Chen, C.-W. Tsai, and J.-W. Yeh, "Effects of Mo, Nb, Ta, Ti, and Zr on mechanical properties of equiatomic Hf-Mo-Nb-Ta-Ti-Zr alloys," Entropy **21**, 15 (2019).

[4] C. Yang, H. Bian, K. Aoyagi, Y. Hayasaka, K. Yamanaka, and A. Chiba, "Synergetic strengthening in HfMoNbTaTi refractory high-entropy alloy via disordered nanoscale phase and semicoherent refractory particle," Mater. Des. **212**, 110248 (2021).

[5] O. N. Senkov, J. M. Scott, S. V. Senkova, D. B. Miracle, and C. F. Woodward, "Microstructure and room temperature properties of a high-entropy TaNbHfZrTi alloy," J. Alloys Compd. **509**, 6043–6048 (2011).

[6] O. N. Senkov, J. M. Scott, S. V. Senkova, F. Meisenkothen, D. B. Miracle, and C. F. Woodward, "Microstructure and elevated temperature properties of a refractory TaNbHfZrTi alloy," J. Mater. Sci. **47**, 4062–4074 (2012).

[7] J.-P. Couzinié, L. Lilensten, Y. Champion, G. Dirras, L. Perrière, and I. Guillot, "On the room temperature deformation mechanisms of a TiZrHfNbTa refractory high-entropy alloy," Mater. Sci. Eng.: A **645**, 255–263 (2015).

[8] Z. An, S. Mao, Y. Liu, L. Wang, H. Zhou, B. Gan, Z. Zhang, and X. Han, "A novel HfNbTaTiV high-entropy alloy of superior mechanical properties designed on the principle of maximum lattice distortion," J. Mater. Sci. Technol. **79**, 109–117 (2021).

[9] H. Y. Yasuda, Y. Yamada, K. Cho, and T. Nagase, "Deformation behavior of HfNbTaTiZr high entropy alloy singe crystals and polycrystals," Mater. Sci. Eng.: A **809**, 140983 (2021).

[10] J. B. Lambert, "Refractory metals and alloys," in *ASM Handbook Volume 2: Properties and Selection: Nonferrous Alloys and Special-Purpose Materials* (ASM International, 1990).

[11] R. I. Zainullin, A. A. Ganeev, R. V. Shakhov, S. K. Mukhtarov, V. M. Imayev, and R. M. Imayev, "Microstructure and mechanical properties of a nickel-base superalloy heavily alloyed with substitution elements," IOP Conf. Ser.: Mater. Sci. Eng. **1008**, 012008 (2020).

[12] C.-C. Juan, M.-H. Tsai, C.-W. Tsai, W.-L. Hsu, C.-M. Lin, S.-K. Chen, S.-J. Lin, and J.-W. Yeh, "Simultaneously increasing the strength and ductility of a refractory high-entropy alloy via grain refining," Mater. Lett. **184**, 200–203 (2016).

[13] O. N. Senkov, A. L. Pilchak, and S. L. Semiatin, "Effect of cold deformation and annealing on the microstructure and tensile properties of a HfNbTaTiZr refractory high entropy alloy," Metall. Mater. Trans. A **49**, 2876–2892 (2018).

[14] S. Y. Chen, L. Wang, W. D. Li, Y. Tong, K. K. Tseng, C. W. Tsai, J. W. Yeh, Y. Ren, W. Guo, J. D. Poplawsky, and P. K. Liaw, "Peierls barrier characteristic and anomalous strain hardening provoked by dynamic-strain-aging strengthening in a body-centered-cubic high-entropy alloy," Mater. Res. Lett. **7**, 475–481 (2019).

[15] S.-P. Wang, E. Ma, and J. Xu, "New ternary equi-atomic refractory medium-entropy alloys with tensile ductility: Hafnium versus titanium into NbTa-based solution," Intermetallics **107**, 15–23 (2019).

[16] L. Lilensten, J.-P. Couzinié, J. Bourgon, L. Perrière, G. Dirras, F. Prima, and I. Guillot, "Design and tensile properties of a bcc Ti-rich high-entropy alloy with transformation-induced plasticity," Mater. Res. Lett. **5**, 110–116 (2017).

[17] Y. D. Wu, Y. H. Cai, T. Wang, J. J. Si, J. Zhu, Y. D. Wang, and X. D. Hui, "A refractory $Hf_{25}Nb_{25}Ti_{25}Zr_{25}$ high-entropy alloy with excellent structural stability and tensile properties," Mater. Lett. **130**, 277–280 (2014).

[18] Z. Lei, X. Liu, Y. Wu, H. Wang, S. Jiang, S. Wang, X. Hui, Y. Wu, B. Gault, P. Kontis, D. Raabe, L. Gu, Q. Zhang, H. Chen, H. Wang, J. Liu, K. An, Q. Zeng, T.-G. Nieh, and Z. Lu, "Enhanced strength and ductility in a high-entropy alloy via ordered oxygen complexes," Nature **563**, 546–550 (2018).

[19] H. Huang, Y. Wu, J. He, H. Wang, X. Liu, K. An, W. Wu, and Z. Lu, "Phase-transformation ductilization of brittle high-entropy alloys via metastability engineering," Adv. Mater. **29**, 1701678 (2017).

[20] X.-G. Li, C. Chen, H. Zheng, Y. Zuo, and S. P. Ong, "Complex strengthening mechanisms in the NbMoTaW multi-principal element alloy," npj Comput. Mater. **6**, 70 (2020).

[21] L. Zhao, H. Zong, X. Ding, and T. Lookman, "Anomalous dislocation core structure in shock compressed bcc high-entropy alloys," Acta Mater. **209**, 116801 (2021).

[22] E. Antillon, C. Woodward, S. I. Rao, and B. Akdim, "Chemical short range order strengthening in BCC complex concentrated alloys," Acta Mater. **215**, 117012 (2021).

[23] S. Yin, Y. Zuo, A. Abu-Odeh, H. Zheng, X.-G. Li, J. Ding, S. P. Ong, M. Asta, and R. O. Ritchie, "Atomistic simulations of dislocation mobility in refractory high-entropy alloys and the effect of chemical short-range order," Nat. Commun. **12**, 4873 (2021).

[24] S. Mishra, S. Maiti, and B. Rai, "Computational property predictions of Ta-Nb-Hf-Zr high-entropy alloys," Sci. Rep. **11**, 4815 (2021).

[25] W. Li, J. Tang, Q. Wang, and H. Fan, "Molecular dynamics simulations on the mechanical behavior of $AlCoCrCu_{0.5}FeNi$ high-entropy alloy nanopillars," in TMS 2019 148th Annual Meeting & Exhibition Supplemental Proceedings, The Minerals, Metals & Materials Series (Springer International Publishing, Cham, 2019), pp. 1271–1280.

[26] S. Feng, L. Li, K. C. Chan, L. Zhao, S. Pan, L. Wang, and R. Liu, "Tuning deformation behavior of $Cu_{0.5}CoNiCrAl$ high-entropy alloy via cooling rate gradient: An atomistic study," Intermetallics **112**, 106553 (2019).

[27] M. Bahramyan, R. Taherzadeh Mousavian, and D. Brabazon, "Determination of atomic-scale structure and compressive behavior of solidified $Al_xCrCoFeCuNi$ high entropy alloys," Int. J. Mech. Sci. **171**, 105389 (2020).

[28]M. Bahramyan, R. T. Mousavian, and D. Brabazon, "Study of the plastic deformation mechanism of TRIP-TWIP high entropy alloys at the atomic level," Int. J. Plast. **127**, 102649 (2020).
[29]Q. Zhang, R. Huang, X. Zhang, T. Cao, Y. Xue, and X. Li, "Deformation mechanisms and remarkable strain hardening in single-crystalline high-entropy-alloy micropillars/nanopillars," Nano Lett. **21**, 3671–3679 (2021).
[30]J. Peng, L. Li, F. Li, B. Liu, S. Zherebtsov, Q. Fang, J. Li, N. Stepanov, Y. Liu, F. Liu, and P. K. Liaw, "The predicted rate-dependent deformation behaviour and multistage strain hardening in a model heterostructured body-centered cubic high entropy alloy," Int. J. Plast. **145**, 103073 (2021).
[31]P. Singh, A. Sharma, A. V. Smirnov, M. S. Diallo, P. K. Ray, G. Balasubramanian, and D. D. Johnson, "Design of high-strength refractory complex solid-solution alloys," npj Comput. Mater. **4**, 16 (2018).
[32]A. Sharma, P. Singh, T. Kirk, V. I. Levitas, P. K. Liaw, G. Balasubramanian, R. Arroyave, and D. D. Johnson, "Pseudoelastic deformation in Mo-based refractory multi-principal element alloys," Acta Mater. **220**, 117299 (2021).
[33]Z. H. Aitken and Y.-W. Zhang, "Revealing the deformation twinning nucleation mechanism of BCC HEAs," MRS Comm. **9**, 406–412 (2019).
[34]X. Huang, L. Liu, X. Duan, W. Liao, J. Huang, H. Sun, and C. Yu, "Atomistic simulation of chemical short-range order in HfNbTaZr high entropy alloy based on a newly-developed interatomic potential," Mater. Des. **202**, 109560 (2021).
[35]S. Xu, S. Z. Chavoshi, and Y. Su, "On calculations of basic structural parameters in multi-principal element alloys using small atomistic models," Comput. Mater. Sci. **202**, 110942 (2022).
[36]R. A. Romero, S. Xu, W.-R. Jian, I. J. Beyerlein, and C. V. Ramana, "Atomistic simulations of the local slip resistances in four refractory multi-principal element alloys," Int. J. Plast. **149**, 103157 (2022).
[37]G. Dirras, L. Lilensten, P. Djemia, M. Laurent-Brocq, D. Tingaud, J.-P. Couzinié, L. Perrière, T. Chauveau, and I. Guillot, "Elastic and plastic properties of as-cast equimolar TiHfZrTaNb high-entropy alloy," Mater. Sci. Eng.: A **654**, 30–38 (2016).
[38]É. Fazakas, V. Zadorozhnyy, L. K. Varga, A. Inoue, D. V. Louzguine-Luzgin, F. Tian, and L. Vitos, "Experimental and theoretical study of $Ti_{20}Zr_{20}Hf_{20}Nb_{20}X_{20}$ (X = V or Cr) refractory high-entropy alloys," Int. J. Refract. Met. Hard Mater. **47**, 131–138 (2014).
[39]H. Song, F. Tian, Q.-M. Hu, L. Vitos, Y. Wang, J. Shen, and N. Chen, "Local lattice distortion in high-entropy alloys," Phys. Rev. Mater. **1**, 023404 (2017).
[40]S. Li, X. Ni, and F. Tian, "*Ab initio* predicted alloying effects on the elastic properties of $Al_xHf_{1-x}NbTaTiZr$ high entropy alloys," Coatings **5**, 366–377 (2015).
[41]S. Xu, E. Hwang, W.-R. Jian, Y. Su, and I. J. Beyerlein, "Atomistic calculations of the generalized stacking fault energies in two refractory multi-principal element alloys," Intermetallics **124**, 106844 (2020).
[42]M. S. Daw and M. I. Baskes, "Embedded-atom method: Derivation and application to impurities, surfaces, and other defects in metals," Phys. Rev. B **29**, 6443–6453 (1984).
[43]S. I. Rao, C. Woodward, B. Akdim, O. N. Senkov, and D. Miracle, "Theory of solid solution strengthening of BCC chemically complex alloys," Acta Mater. **209**, 116758 (2021).
[44]X. W. Zhou, R. A. Johnson, and H. N. G. Wadley, "Misfit-energy-increasing dislocations in vapor-deposited CoFe/NiFe multilayers," Phys. Rev. B **69**, 144113 (2004).
[45]D.-Y. Lin, S. S. Wang, D. L. Peng, M. Li, and X. D. Hui, "An *n*-body potential for a Zr-Nb system based on the embedded-atom method," J. Phys.: Condens. Matter **25**, 105404 (2013).
[46]R. A. Johnson, "Alloy models with the embedded-atom method," Phys. Rev. B **39**, 12554–12559 (1989).
[47]X. W. Zhou, H. N. G. Wadley, R. A. Johnson, D. J. Larson, N. Tabat, A. Cerezo, A. K. Petford-Long, G. D. W. Smith, P. H. Clifton, R. L. Martens, and T. F. Kelly, "Atomic scale structure of sputtered metal multilayers," Acta Mater. **49**, 4005–4015 (2001).
[48]R. W. Smith and G. S. Was, "Application of molecular dynamics to the study of hydrogen embrittlement in Ni-Cr-Fe alloys," Phys. Rev. B **40**, 10322–10336 (1989).
[49]S. Plimpton, "Fast parallel algorithms for short-range molecular dynamics," J. Comput. Phys. **117**, 1–19 (1995).
[50]G. Kresse and J. Furthmüller, "Efficient iterative schemes for *ab initio* total-energy calculations using a plane-wave basis set," Phys. Rev. B **54**, 11169–11186 (1996).
[51]D. Roundy, C. R. Krenn, M. L. Cohen, and J. W. Morris, "Ideal shear strengths of fcc aluminum and copper," Phys. Rev. Lett. **82**, 2713–2716 (1999).
[52]S. Ogata, J. Li, and S. Yip, "Ideal pure shear strength of aluminum and copper," Science **298**, 807–811 (2002).
[53]M. Jahnátek, J. Hafner, and M. Krajčí, "Shear deformation, ideal strength, and stacking fault formation of fcc metals: A density-functional study of Al and Cu," Phys. Rev. B **79**, 224103 (2009).
[54]S. Ogata, J. Li, N. Hirosaki, Y. Shibutani, and S. Yip, "Ideal shear strain of metals and ceramics," Phys. Rev. B **70**, 104104 (2004).
[55]S. L. Shang, W. Y. Wang, Y. Wang, Y. Du, J. X. Zhang, A. D. Patel, and Z. K. Liu, "Temperature-dependent ideal strength and stacking fault energy of fcc Ni: A first-principles study of shear deformation," J. Phys.: Condens. Matter **24**, 155402 (2012).
[56]X. Li, S. Schönecker, W. Li, L. K. Varga, D. L. Irving, and L. Vitos, "Tensile and shear loading of four fcc high-entropy alloys: A first-principles study," Phys. Rev. B **97**, 094102 (2018).
[57]D. Roundy, C. R. Krenn, M. L. Cohen, and J. W. Morris, "The ideal strength of tungsten," Philos. Mag. A **81**, 1725–1747 (2001).
[58]S. H. Zhang, Z. H. Fu, and R. F. Zhang, "ADAIS: Automatic derivation of anisotropic ideal strength via high-throughput first-principles computations," Comput. Phys. Commun. **238**, 244–253 (2019).
[59]L. Lilensten, J.-P. Couzinié, L. Perrière, A. Hocini, C. Keller, G. Dirras, and I. Guillot, "Study of a bcc multi-principal element alloy: Tensile and simple shear properties and underlying deformation mechanisms," Acta Mater. **142**, 131–141 (2018).
[60]S. Xu, Y. Su, W.-R. Jian, and I. J. Beyerlein, "Local slip resistances in equal-molar MoNbTi multi-principal element alloy," Acta Mater. **202**, 68–79 (2021).
[61]S. Xu, W.-R. Jian, Y. Su, and I. J. Beyerlein, "Line-length-dependent dislocation glide in refractory multi-principal element alloys," Appl. Phys. Lett. **120**, 061901 (2022).
[62]A. Zunger, S.-H. Wei, L. G. Ferreira, and J. E. Bernard, "Special quasirandom structures," Phys. Rev. Lett. **65**, 353–356 (1990).
[63]A. van de Walle, P. Tiwary, M. de Jong, D. L. Olmsted, M. Asta, A. Dick, D. Shin, Y. Wang, L.-Q. Chen, and Z.-K. Liu, "Efficient stochastic generation of special quasirandom structures," Calphad **42**, 13–18 (2013).
[64]A. Stukowski, "Visualization and analysis of atomistic simulation data with OVITO—The Open Visualization Tool," Modell. Simul. Mater. Sci. Eng. **18**, 015012 (2010).
[65]W.-R. Jian, Z. Xie, S. Xu, Y. Su, X. Yao, and I. J. Beyerlein, "Effects of lattice distortion and chemical short-range order on the mechanisms of deformation in medium entropy alloy CoCrNi," Acta Mater. **199**, 352–369 (2020).
[66]B. Sadigh, P. Erhart, A. Stukowski, A. Caro, E. Martinez, and L. Zepeda-Ruiz, "Scalable parallel Monte Carlo algorithm for atomistic simulations of precipitation in alloys," Phys. Rev. B **85**, 184203 (2012).
[67]J. M. Cowley, "An approximate theory of order in alloys," Phys. Rev. **77**, 669 (1950).
[68]D. de Fontaine, "The number of independent pair-correlation functions in multicomponent systems," J. Appl. Crystallogr. **4**, 15–19 (1971).
[69]B. Joós and M. S. Duesbery, "The Peierls stress of dislocations: An analytic formula," Phys. Rev. Lett. **78**, 266–269 (1997).
[70]X. Wang, S. Xu, W.-R. Jian, X.-G. Li, Y. Su, and I. J. Beyerlein, "Generalized stacking fault energies and Peierls stresses in refractory body-centered cubic metals from machine learning-based interatomic potentials," Comput. Mater. Sci. **192**, 110364 (2021).
[71]S. Zhao, Y. Osetsky, G. M. Stocks, and Y. Zhang, "Local-environment dependence of stacking fault energies in concentrated solid-solution alloys," npj Comput. Mater. **5**, 13 (2019).

[72]S. Zhao, "Fluctuations in stacking fault energies improve irradiation tolerance of concentrated solid-solution alloys," J. Nucl. Mater. **530**, 151886 (2020).
[73]O. N. Senkov and S. L. Semiatin, "Microstructure and properties of a refractory high-entropy alloy after cold working," J. Alloys Compd. **649**, 1110–1123 (2015).
[74]W. Wu, S. Ni, Y. Liu, and M. Song, "Effects of cold rolling and subsequent annealing on the microstructure of a HfNbTaTiZr high-entropy alloy," J. Mater. Res. **31**, 3815–3823 (2016).
[75]B. Schuh, B. Völker, J. Todt, N. Schell, L. Perrière, J. Li, J. P. Couzinié, and A. Hohenwarter, "Thermodynamic instability of a nanocrystalline, single-phase TiZrNbHfTa alloy and its impact on the mechanical properties," Acta Mater. **142**, 201–212 (2018).
[76]S. Y. Chen, Y. Tong, K.-K. Tseng, J.-W. Yeh, J. D. Poplawsky, J. G. Wen, M. C. Gao, G. Kim, W. Chen, Y. Ren, R. Feng, W. D. Li, and P. K. Liaw, "Phase transformations of HfNbTaTiZr high-entropy alloy at intermediate temperatures," Scr. Mater. **158**, 50–56 (2019).
[77]N. D. Stepanov, N. Y. Yurchenko, S. V. Zherebtsov, M. A. Tikhonovsky, and G. A. Salishchev, "Aging behavior of the HfNbTaTiZr high entropy alloy," Mater. Lett. **211**, 87–90 (2018).
[78]M. C. Gao and D. E. Alman, "Searching for next single-phase high-entropy alloy compositions," Entropy **15**, 4504–4519 (2013).
[79]X. Huang, L. Liu, W. Liao, J. Huang, H. Sun, and C. Yu, "Characterization of nucleation behavior in temperature-induced BCC-to-HCP phase transformation for high entropy alloy," Acta Metall. Sin. **34**, 1546–1556 (2021).
[80]S.-M. Chen, Z.-J. Ma, S. Qiu, L.-J. Zhang, S.-Z. Zhang, R. Yang, and Q.-M. Hu, "Phase decomposition and strengthening in HfNbTaTiZr high entropy alloy from first-principles calculations," Acta Mater. **225**, 117582 (2022).
[81]A. Stukowski, "Structure identification methods for atomistic simulations of crystalline materials," Modell. Simul. Mater. Sci. Eng. **20**, 045021 (2012).
[82]T. Ruan, B. Wang, C. Xu, and Y. Jiang, "Shear deformation helps phase transition in pure iron thin films with 'inactive' surfaces: A molecular dynamics study," Crystals **10**, 855 (2020).
[83]S. Maiti and W. Steurer, "Structural-disorder and its effect on mechanical properties in single-phase TaNbHfZr high-entropy alloy," Acta Mater. **106**, 87–97 (2016).
[84]Z. Xie, W.-R. Jian, S. Xu, I. J. Beyerlein, X. Zhang, X. Yao, and R. Zhang, "Phase transition in medium entropy alloy CoCrNi under quasi-isentropic compression," Int. J. Plast. **157**, 103389 (2022).
[85]H. Zheng, L. T. Fey, X.-G. Li, Y.-J. Hu, L. Qi, C. Chen, S. Xu, I. J. Beyerlein, and S. P. Ong, "Multi-scale investigation of chemical short range order and dislocation glide in the MoNbTi and TaNbTi refractory multi-principal element alloys," arXiv (2022).